Supplementary Discussion

Theoretical underpinnings. Many theoretical studies on the motion of microorganisms have been revisited since Gray and Hancock used the resistive-force theory (RFT) to predict the swimming speed of sea-urchin spermatozoa[S1]. Most theoretical models of microorganisms have been focused on swimming *E. coli* at very low Reynolds numbers ($Re \approx 10^{-4}$). Some of that work was driven by interest in understanding the behavior of the rotating flagella for applications to bio-mimetic vehicles in very viscous media, and the behavior of the microorganisms near wall boundaries because this behavior is related to biofilm formation and pathogenic infections[S2-S4]. Recently, both theoretical[S5] and computational[S6, S7] studies of the swimming of an *E. coli* cell have been built using RFT and showed the behavior of the microorganisms (a circular clock-wise trajectory) near wall boundaries. For these computational swimming models, the Stokes equations were solved for the fluid because bacteria swim at very low Reynolds numbers. For the cell simulations using only RFT described above, the force and torque on the cell body and flagella were required to be in equilibrium[S6, S7].

The numerical studies presented here simulating individual bacterium motion apply Lagrangian methods and rigid body dynamics to the design a microfluidic device to trap single bacterium in specific locations. Our computational model is different from the above mentioned computational swimming models[S6,S7] in several respects. Since the bacteria in our device are introduced using pressure driven flow, the flow speed of the bacteria in our model (~4 mm/s) is much higher than in the swimming model (~10 μm/s). Consequently, the Reynolds number ($Re \approx 10^{-2}$) in our model is higher than that used in swimming models ($Re \approx 10^{-4}$). In our model, the Navier-Stokes equations including convective terms were solved for the fluid first. Then Newtonian equations of translational and rotational motions with mass inertia terms for the motion of a single bacterial cell were one-way coupled with the pre-solved flow fields. Here, the effects of bacteria swimming were considered to be negligible due to both the higher Reynolds number conditions and our experimental observations; as ellipsoidal cells approach the wall of the obstacle, the high shear rate in the near-wall region results in high velocity cell rotation (**Supplementary Movies 2-5**). It has been reported that hydrodynamic high shear stresses influence motion by biasing the cell's

direction[S8-S10]. Furthermore, our simulated results also show ellipsoidal bacteria flipping with respect to positive x rotational axis soon after passing the edge of a sieve. The simulations and experiments agree in this respect.

Further simulated data (**Supplementary Fig.2**) shows an ellipsoidal cell flipping over after it detours around S8 (it rotates in the opposite direction of its initial orientation after t= 50 ms). This result is supported by the data (**Supplementary Fig.2**), showing the increase of translational velocity in the $\hat{x}_2$ directions at t=55 ms, and simultaneous steep variations of the orientation components in the x_1 and x_2 directions. The high magnitudes of $O_{x_1}^p$ and $O_{x_3}^p$ (approximately ±1) indicates that the major axis of symmetry of the ellipsoidal cell is perpendicular to the direction of flow, and the cell moves in the direction of the minor axis of the ellipsoid; this motion pattern was observed at t= 56 ms. Thus, it sees a higher hydrodynamic resistance force than a cell with high magnitude of $O_{x_2}^p$ (the axis of symmetry of the ellipsoidal cell is parallel to the direction of flow). Eventually, a high magnitude of $O_{x_2}^p$ was recovered when the cell exited the circular trapping chamber.

Supplementary Methods

Ellipsoidal *E. coli* Modeling. The detailed modeling of ellipsoidal *E. coli* in the microfluidic device was found in the literature.[S11] To readily understand this modeling, the modeling approach is rephrased as following. The motion of the ellipsoidal *E. coli* in the microfluidic device was simulated using a Lagrangian approach based on one-way coupling between the time dependent particle motion and the pre-computed Newtonian flow fields. The calculation interpolates the flow velocity and velocity gradients at the cell body's center of mass. A microbial cell was assumed to be an elastic ellipsoid with a major length of 4 μm and a minor length of 1 μm. Interactions between moving cells were not considered because the suspension was of a sufficiently low concentration. However, interactions with the channel's surface were considered to both prohibit moving cells from penetrating the computational wall boundary and to describe tumbling motions of *E. coli* on the surface. The forces considered in the equation of translational motion for an ellipsoidal cell were those due to the hydrodynamic drag ($\boldsymbol{F}_H$), pressure gradient ($\boldsymbol{F}_{PG}$), gravity ($\left(m_p - m_f\right)\boldsymbol{g}$), Brownian motion ($\boldsymbol{F}_B$) and collisions between cells ($\boldsymbol{F}_S$) and the surface ($\boldsymbol{F}_W$). In addition, the torques considered in the equations of rotational motion for the ellipsoidal cells were hydrodynamic torque ($\hat{\boldsymbol{T}}_H$) and repulsive torques induced by collisions on the surface ($\hat{\boldsymbol{T}}_W$). The rotational motion equations used to find the angular velocity ($\hat{\boldsymbol{\omega}}_p^*$) of a particle are expressed in the body-space (**Supplementary Figure 3**). Furthermore, one way coupling Lagrangian approach combined with rigid body theory. For the rigid body simulation, the time rate of change of the four Euler parameters (quaternion; $\varepsilon_1, \varepsilon_2, \varepsilon_3, \eta$)[S12] is related to the particle angular velocity. So, the resulting thirteen equations of translational motion equation, rotational motional motion, and rigid body theory for the four Euler parameters are expressed as:

$$m_p \frac{d\boldsymbol{u}_p^*}{dt} = \boldsymbol{F}_H + \boldsymbol{F}_{PG} + \left(m_p - m_f\right)\boldsymbol{g} + \boldsymbol{F}_B + \boldsymbol{F}_S + \boldsymbol{F}_W$$

$$m_p \frac{d\vec{u}_p}{dt} = -\mu \vec{\vec{K}} \cdot \left(\vec{u}_p - \vec{u}_f\right) + m_p \vec{g} + F_{wall} + F_B \qquad (1)$$

$$\frac{d\boldsymbol{x}_p^*}{dt} = \boldsymbol{u}_p^* \tag{2}$$

$$\hat{\boldsymbol{I}}\frac{d\hat{\boldsymbol{\omega}}_p^*}{dt} = \hat{\boldsymbol{I}}\hat{\boldsymbol{\omega}}_p^* \times \hat{\boldsymbol{\omega}}_p^* + \hat{\boldsymbol{T}}_H + \hat{\boldsymbol{T}}_W \tag{3}$$

$$\begin{pmatrix} d\varepsilon_1/dt \\ d\varepsilon_2/dt \\ d\varepsilon_3/dt \\ d\eta/dt \end{pmatrix} = \frac{1}{2}\begin{pmatrix} \eta & -\varepsilon_3 & \varepsilon_2 \\ \varepsilon_3 & \eta & -\varepsilon_1 \\ -\varepsilon_2 & \varepsilon_1 & \eta \\ -\varepsilon_1 & -\varepsilon_2 & -\varepsilon_3 \end{pmatrix} \cdot \hat{\boldsymbol{\omega}}_p . \tag{4}$$

where $\boldsymbol{u}_p^*$ is particle velocity, $\boldsymbol{x}_p^*$ is location vector, $m_p\left(=\frac{4}{3}\pi a^3 \beta \rho_p\right)$, $m_f\left(=\frac{4}{3}\pi a^3 \beta \rho_f\right)$ are the mean masses of the ellipsoidal particle and fluid, respectively. Here, $\beta(=b/a)$ is the ellipsoidal aspect ratio of semi-major (b) and semi-minor (a) axes, and ρ_p and ρ_f are particle density (1040 kg m^{-3}) and fluid density (997.5 kg m^{-3}), respectively. $\hat{\boldsymbol{I}}$ is moment of inertia diagonal matrix in the body frame with elements, $I_{\hat{x}_1}$, $I_{\hat{x}_2}$ and $I_{\hat{x}_3}$ about the principal axes. For the ellipsoidal particle, they are expressed as $I_{\hat{x}_1} = I_{\hat{x}_3} = 0.2\left(1+\beta^2\right)a^2 m_p$, and $I_{\hat{x}_2} = 0.4a^2 m_p$. The detailed explanations of external forces and torques are found in the elsewhere.[S11] Each ellipsoidal cell trajectory was obtained by integrating the thirteen eqs. (1), (2), (3), and (4) under the following initial conditions. The initial cell velocity was interpolated using the fluid velocity at the initial seeding location, and the initial cell angular velocity was set to zero. A fourth order Rosenbrock method based on a adaptive time-stepping technique was utilized as the integration method, as it was more reliable for solving stiff linear equations without divergence than the Runge-Kutta method.[S13]

Device Fabrication. The device patterns were direct-written from Drawing Exchange Format (DXF) drawings onto commercial chrome-on-glass photomask plates (Nanofilm,

Westlake Village, CA) using a DWL66 laser mask writer (Heidelberg Instruments, Heidelberg, Germany). Sub-micron features were achieved using the DWL66's 2 mm focal length write head (**Supplementary Fig. 5**; top). Features of this size required optimizing the exposure of the AZTFP-650 photoresist on the mask. Exposure optimization was generally required for each mask writing session. After writing, the photoresist was developed for 70s using AZ300 MIF developer (MicroChem Corp., Newton, MA) and then the chrome layer was etched for 2 min using Chromium Mask Etchant (Transene, Danvers, MA).

The PDMS devices were generated using conventional photolithography and soft lithography techniques as previously described[S14]. Briefly, patterned silicon wafers were made by applying a layer of SU-8 2010 photoresist (MicroChem Corp., Newton, MA) onto 3-inch silicon wafers (University Wafer, South Boston, MA) using a Delta 80RC spin coater (SUSS MicroTec, Waterbury Center, VT). The wafers were exposed to UV light through the patterned chrome photomask (**Supplementary Fig. 5**; top) using a MA/BA6 mask aligner (SUSS MicroTec, Waterbury Center, VT) and developed using SU-8 developer solution (MicroChem). The patterned wafers (**Supplementary Fig. 5**; bottom) were then silanized using chlorotrimethylsilane (Aldrich, St. Louis, MO) before curing PDMS (Dow Corning, Midland, MI) against the patterned wafer for two hr at 80°C. After curing, the patterned PDMS was removed from the wafer and inlet/outlet ports were punched through the thickness of the PDMS. The PDMS was then gently cleaned with ethanol, dried, and treated with air plasma for 45 s along with a glass coverslip (VWR, West Chester, PA). The PDMS and coverslip were gently pressed together and subsequently baked for 2 hr at 80°C to enhance bonding.

Protocol for *E. coli* Preparations. *E. coli* K-12 were cultured on LB agar plates at 37°C for 24 hr and then stored at 4°C until used. Bacteria were expanded in solution for each experiment by removing a single colony of bacteria from an agar plate with a pipette tip, placing the tip in a test tube containing 2 ml of fresh LB broth, and incubating at 37°C on a shaker plate for 16-18 hr. Following incubation, the *E. coli* concentration was calculated by measuring the optical density of the solution using a spectrophotometer (BioPhotometer, Eppendorf, Westbury, NY) and correlating the measured result with a previously

determined calibration curve. This solution was centrifuged at 10,000 rpm for 60s and the pellet was resuspended in 1 ml of PBS. In order to stain the bacteria for visualization in the microfluidic trapping experiments, 2 ml of LIVE/DEAD bacterial viability staining solution (Invitrogen, San Diego, CA) was added to the resuspended cells, vortexed, and incubated at room temperature for 15 min. Prior to initiating the trapping experiments, the stained bacteria were diluted to a final working concentration of $2x10^7$ CFU/ml in PBS.

Supplementary Figure Captions

Supplementary Figure 1: Temporal data for trap design C. A small number of cells (~1-3 CFU) were locally trapped in the S1 when 1000 CFU was loaded at the inlet for 30 sec. Within 10 s (f=333 CFU), single cell trapping events were observed at S1, S2, S3, and S7. Multiple cells were also trapped at S1 and S2 for the loading times of 20s and 30 s, respectively.

Supplementary Figure 2: Detailed evolution of the cell orientation during its motion for both simulation and experimental data.

Supplementary Figure 3: Fundamentals of the ellipsoidal cell model. A) Schematic of an ellipsoidal cell moving in a global coordinate system (x_1, x_2, x_3), the body-frame $(\hat{x}_1, \hat{x}_2, \hat{x}_3)$, and the motion-frame $(\tilde{x}_1, \tilde{x}_2, \tilde{x}_3)$, B) Euler angles; **N** is the line of nodes, ϕ is the angle between the $\tilde{x}_1$-axis and the line of nodes, θ is the angle between the $\hat{x}_3$-axis and the $\tilde{x}_3$-axis, and φ is the angle between the line of nodes and the $\hat{x}_1$-axis, C) computational model for an ellipsoidal *E-coli* cell with a semi-minor length, a, = 0.5μm and a semi-major length, b = 2μm, which is composed of thirty two beads with radius r_b = 0.285μm and can be constructed using the parameterized formulas: $x = a\sin\sigma\cos\upsilon,\ y = b\sin\upsilon$ and $z = a\cos\sigma\cos\upsilon$ where $0 \le \sigma \le 180,\quad 0 \le \upsilon \le 360,$ and D) a diagram showing translational velocities and rotational angular velocities at discrete times.

Supplementary Figure 4: Trapping performance for each sieve individually.

Supplementary Figure 5: Finite volume meshes for the fluid model. Right panels show close up views of the mesh optimization for each aperture type.

Supplementary Figure 6: Device fabrication process. Top: images of the chrome masks used to make each of the three devices. Bottom, images of the SU-8 masters used to cast the PDMS parts.

Supplementary References

S1. Gray, J., Hancock, G.J. The propulsion of sea-urchin spermatozoa. J. Exp. Biol. 32, 802–814 (1955).

S2. Ottemann, K.M., Miller, J.F. Roles for motility in bacterial-host interactions. Mol. Microbiol. 24, 1109–1117 (1997).

S3. Pratt, L.A., Kolter, R. Genetic analysis of *Escherichia coli* biofilm formation: roles of flagella, motility, chemotaxis and Type I pili. Mol. Microbiol. 30, 285–293 (1998).

S4. Cogan, N.G. Two-fluid model of biofilm disinfection. Bull. Math. Biol. 70, 800–819 (2008).

S5. Lauga, E., DiLuzio, W.R., Whitesides, G.M. & Stone, H.A. Swimming in circles: motion of bacteria near solid boundaries. Biophys. J. 90, 400–412 (2006).

S6. Ramia, M., Tullock, D.L. & Phan-Thien, N. The role of hydrodynamic interaction in the locomotion of microorganisms. Biophys. J. 65, 755–778 (1993).

S7. Goto, T., Nakata, K., Baba, K., Nishimura, M., & Magariyamay, Y. A fluid-dynamic interpretation of the asymmetric motion of singly flagellated bacteria swimming close to a boundary. Biophys. J. 89, 3771–3779 (2005).

S8. Jeffrey, G.B. The motion of ellipsoidal particles immersed in a viscous fluid. Proc. R. Soc. A 102, 161 (1922).

S9. Walker, G.M. et al. Effects of flow and diffusion on chemotaxis studies in microfabricated gradient generator. Lab Chip 5, 611–618 (2005).

S10. Marcos & Stocker, R. Microorganisms in vortices: a microfluidic setup. Limnol. Oceanogr. 4, 392–398 (2006).

S11. Kim, M. C. & Klapperich C. M. A new method for simulating individual ellipsoidal bacteria in

microfluidic devices. *Lab Chip.* Accepted (2010).

S12. Goldstein, H. *Classical Mechanics*, 2nd Ed. (Addison-Wesley, Reading, MA, 1980).

S13. Press, W.H., Teukolsky, S.A. & Flannery, B.P. *Numerical Recipes in C.* (Cambridge University Press, Cambridge, 1992).

S14. Xia, Y., Whitesides, G. M. Soft Lithography. *Annu. Rev. Mater. Sci.* 28, 153-184 (1998).

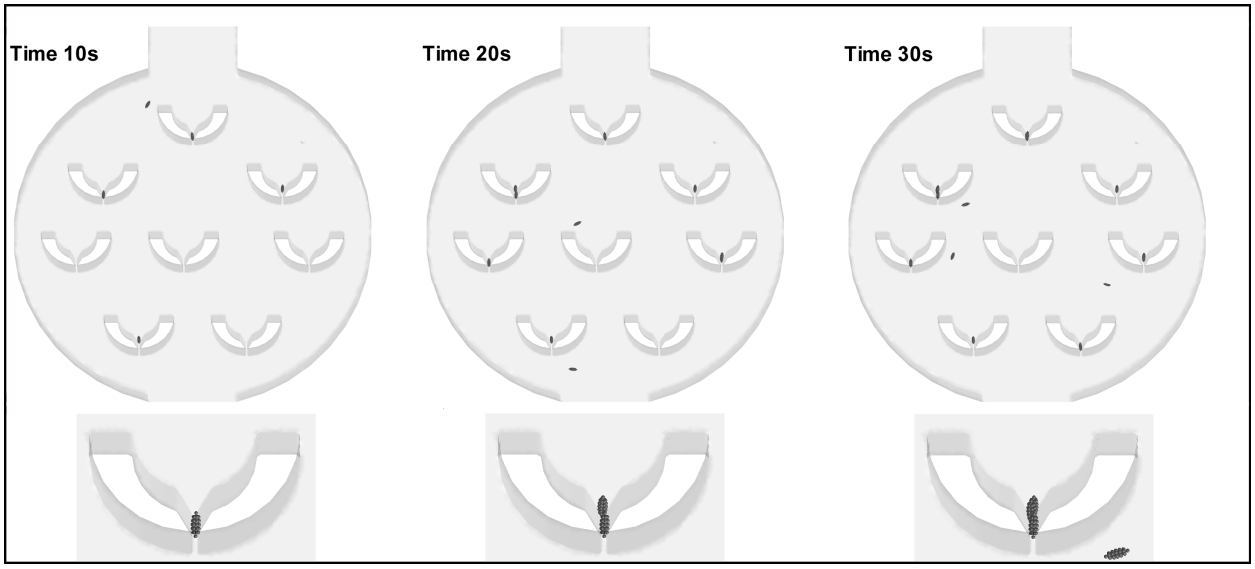

Supp. Figure 1

Supplementary Material (ESI) for Lab on a Chip

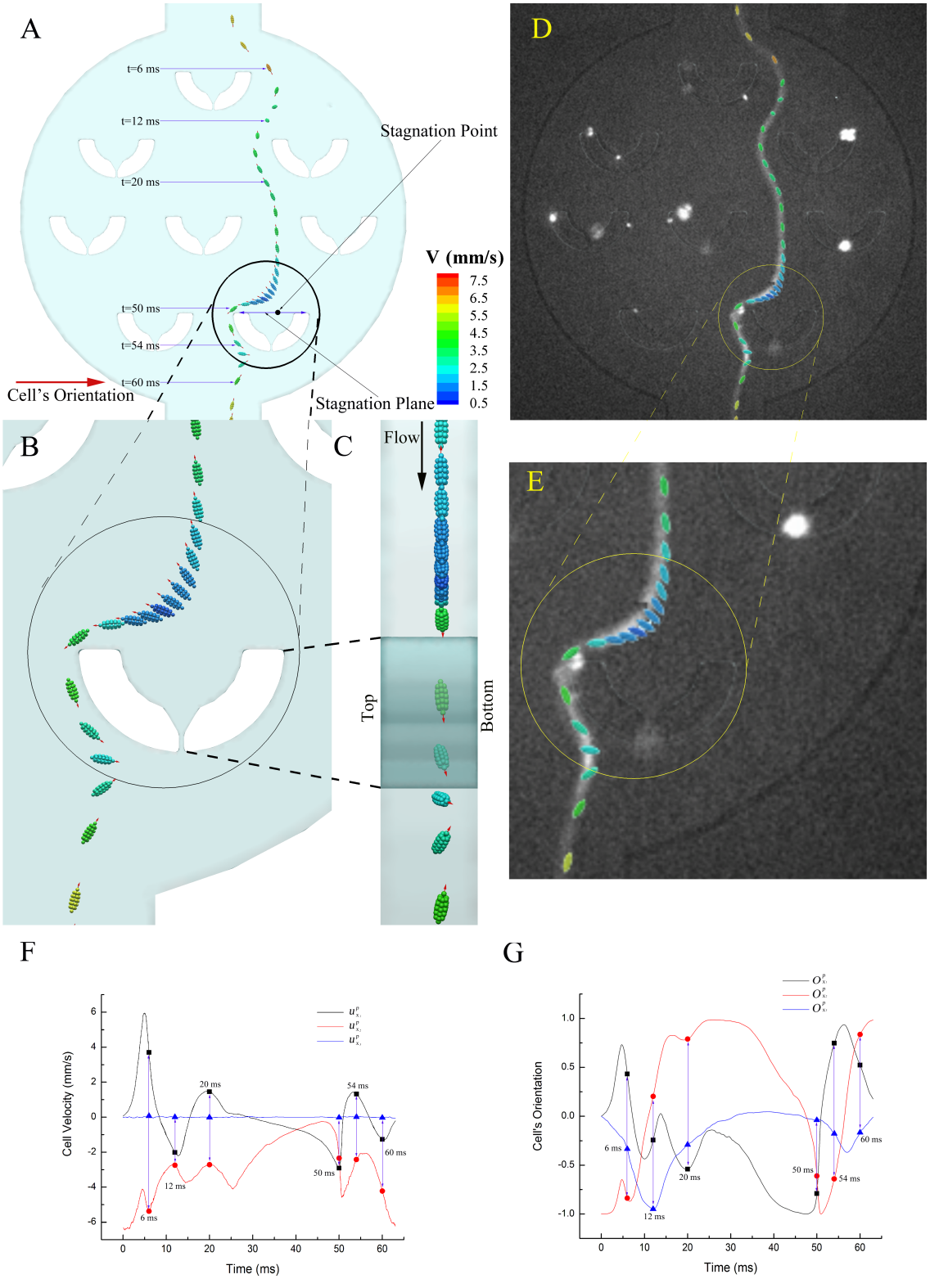

Supp Figure 2

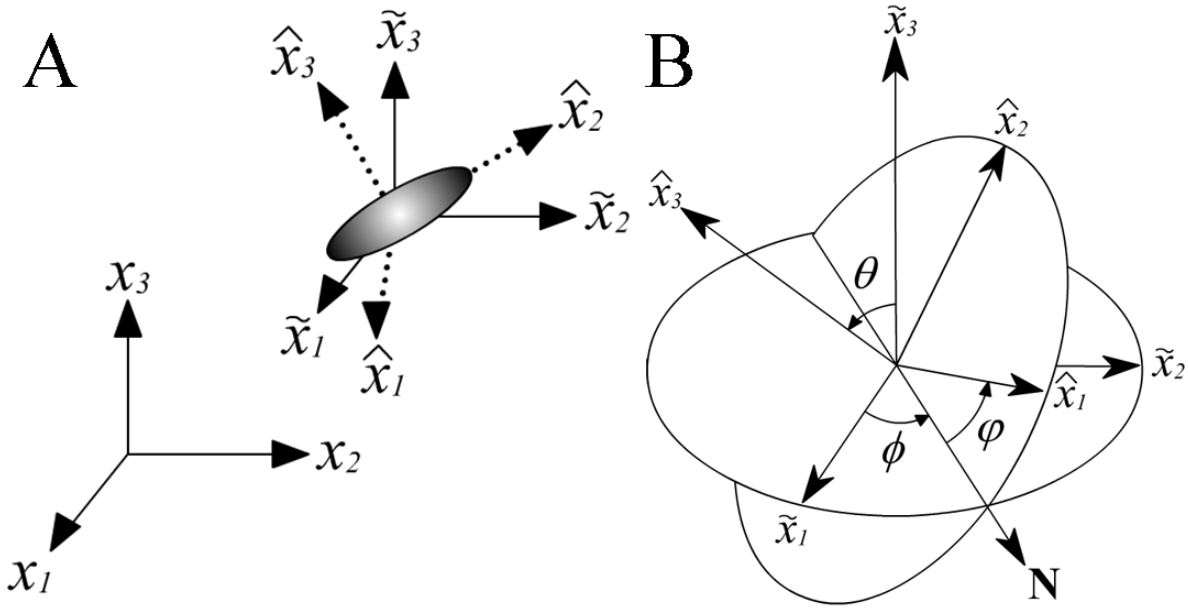

Supp Figure 3

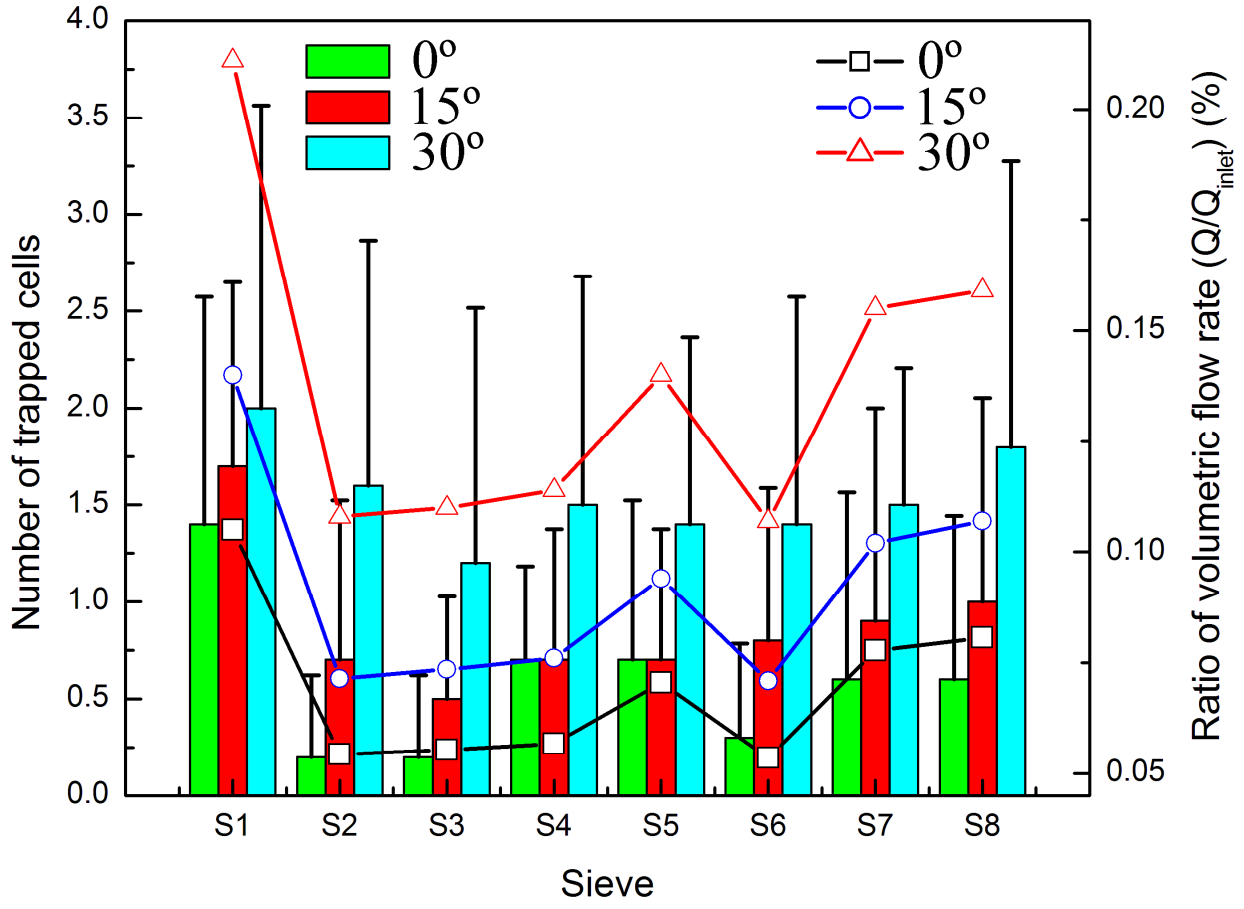

Supp Figure 4

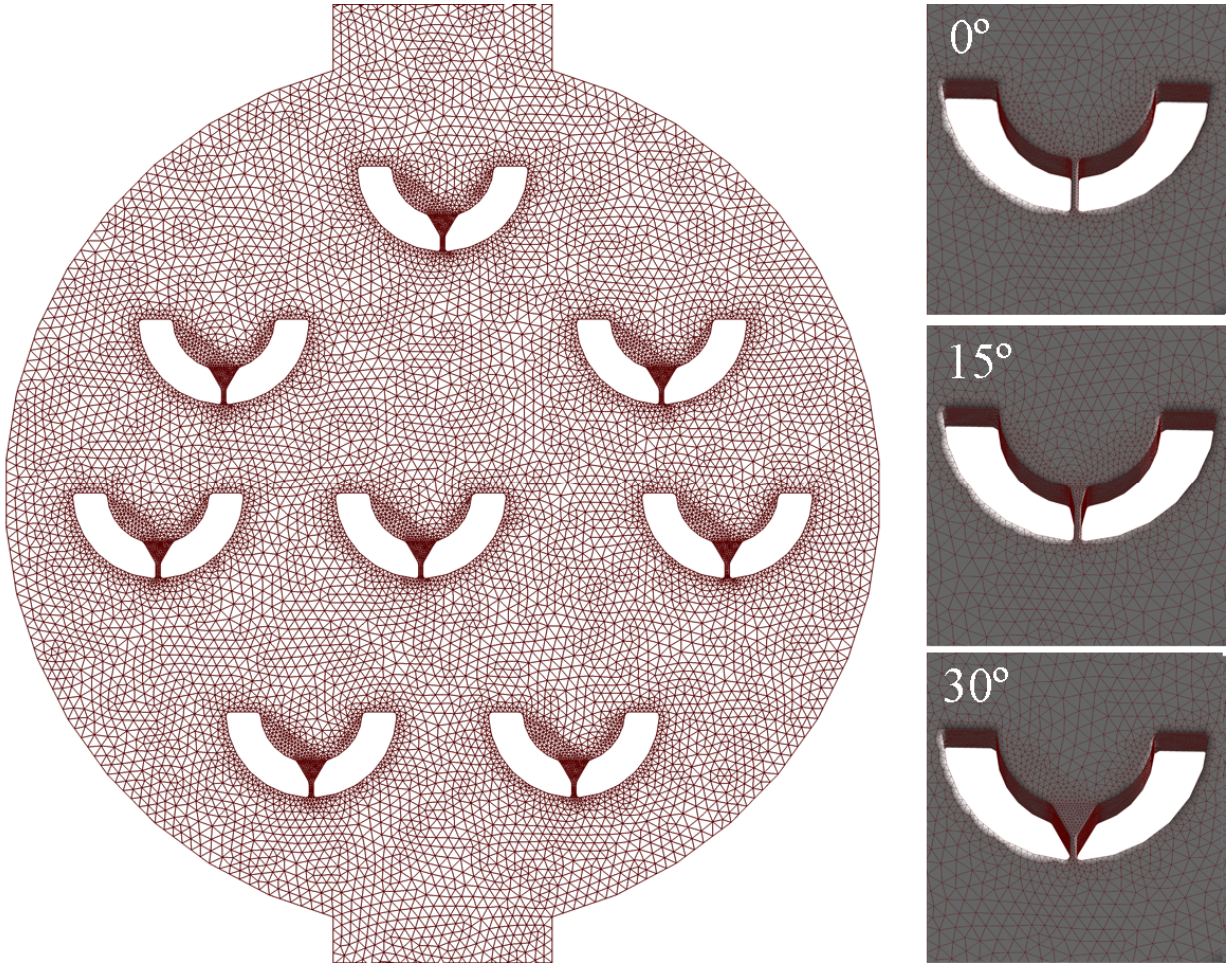

Supp Figure 5

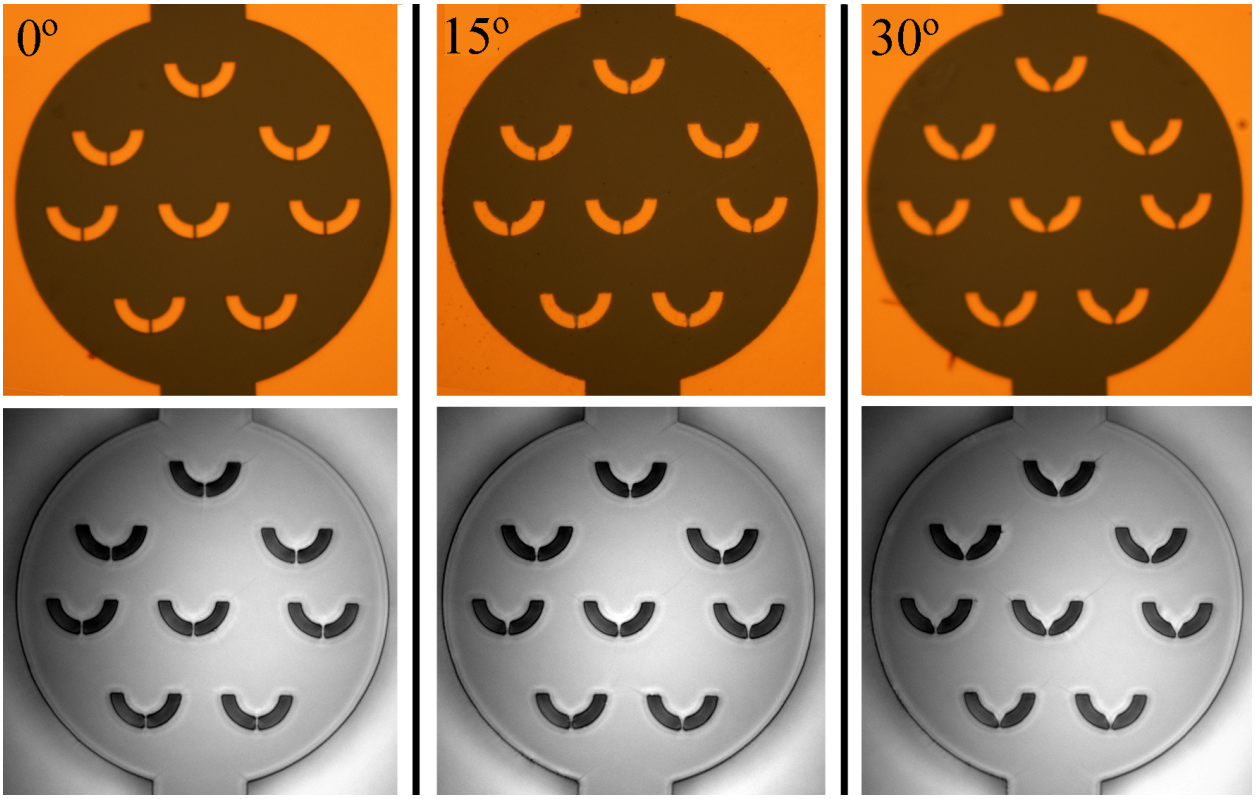

Supp Figure 6